# E 3 Principles of Active Matter

Roland G. Winkler
Theoretical Soft Matter and Biophysics
Institute for Advanced Simulation
Forschungszentrum Jülich GmbH

## Contents



Lecture Notes of the $49^{\text{th}}$ IFF Spring School "Physics of Life" (Forschungszentrum Jülich, 2018). 

# 1 Introduction

Active matter, whose constituents (agents) consume internal energy or extract energy from the environment and are thus far from thermal equilibrium, comprises a vast range of systems ranging from the nano- and microscale up to macroscopic length scales (cf. Fig. 1) [1–5]. On the nanoscale, proteins and other macromolecules in the interior of a cell undergo cyclic conformational changes and stir the surrounding fluid [6, 7]. Since the appearing fluctuating flows are non-thermal, work can be performed by extraction of energy leading to, e.g., an enhanced diffusive motion [6, 8] and chemotaxis [9]. In motility assays, biological semiflexible polar filaments, such as actin and microtubules, are propelled on carpets of motor proteins anchored on a substrate, which results in a directed motion [10–17]. Propulsion of such biological filaments in the cell cytoskeleton due to tread-milling and dimeric or tetrameric motor proteins is ubiquitous. Mixtures of active and passive components are a characteristics of eukaryotic cells with the active cytoskeleton on the one hand and an embedded large variety of passive colloidal and polymeric objects on the other hand. Here, an enhanced random motion of tracer particles has been observed [18]. Moreover, an influence of the active microtubule [19] or actin-filament [20] dynamics on the motion of chromosomal loci [21, 22] or that of chromatin has been found [23].
On larger scales, there is plethora of biological microswimmers such as spermatozoa, bacteria, protozoa, and algae [2]. They use flagella—whip-like structures protruding from their bodies—for their propulsion (cf. Fig. 1). Swimming of uni- and multicellular organisms is essential for their search for food (chemotaxis), the reaction to light (phototaxis), the orientation in the gravitation field (gravitaxis), or for reproduction [2,24]. A paradigmatic example is *Escherichia coli* (*E. coli*), which propels itself by helical filaments (cf. Fig. 1). A flagellum is rotated by a motor complex consisting of several proteins, and is anchored in the bacterial cell wall [25,26]. The (counterclock-wise) rotating flagella self-organize in helical bundle(s), which push the cell forward [24, 27, 28]. *E. coli* and other bacteria swim in a "run-and- tumble" motion, where they change the rotation direction of some or all flagella, which results in a deterioration of the bundle and a reorientation (tumble) [25, 29, 30]. By returning to the original rotation direction, the bundle is reestablished and the bacterium swims again (run). This leads to a diffusive motion determined by the activity of the cell on long time scales.
Flagellated microorganisms not only swim as individuals, but exhibit collective behavior at a surface or in a thin liquid film in form of swarming [2]. Here, bacteria cooperativity reaches a new level as they exhibit highly organized movements with remarkable large-scale patterns such as networks, complex vortices, swarms, or turbulence [31, 32]. Remarkably, similar collective phenomena are observed by active systems on the macroscale such as schools of fish, flocks of birds (cf. Fig. 1), mammalian herds, or crowds of humans [33].
Aside from biological active matter, the design of artificial nano- and microswimmers is highly desirable to perform a multitude of tasks in technical and medical applications. Consequently, various design strategies are explored and different propulsion mechanisms have been proposed [2, 3, 34]. In particular, experimental studies on self-propelled Janus particles and computer simulations reveal motility induced cluster formation and phase separation (MIPS) [2,3,35–42] (cf. Fig. 1).
The physics ruling activity and swimming on the micrometer scale is very different from that applying to the macroworld. Swimming at the micrometer scale is swimming at low Reynolds numbers, where viscous damping by far dominates over inertia [43]. Hence, swimming concepts of the high-Reynolds number macroworld are ineffective on small scales. In the evolutionary process, microorganisms acquired propulsion strategies, which successfully overcome

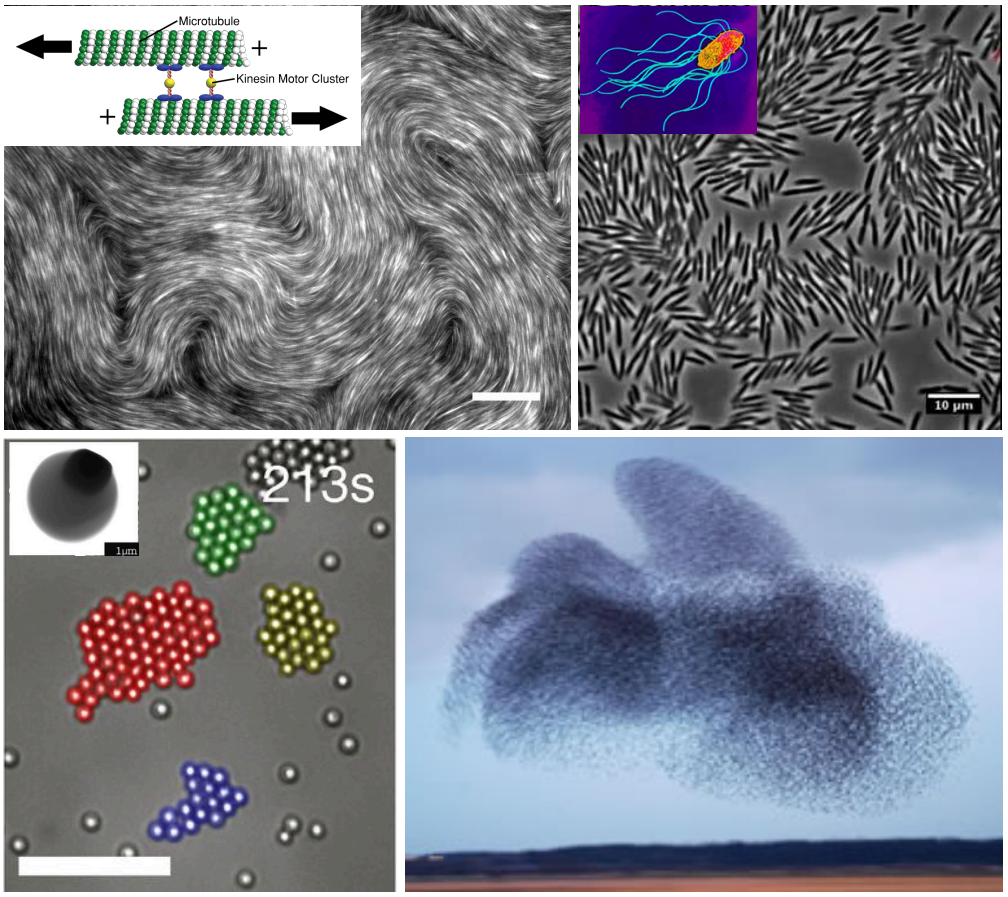


**Fig. 1:** *(Top left) An active nematic liquid of filamentous microtubules driven by molecular motors exhibits collectively drive mesoscale turbulent-like dynamics [44, 45]. (Top right) Swarming* E. coli *bacteria [46]. The inset shows a* Salmonella enterica *with the cylindrical cell body and several flagella [47]. (Bottom left) Living crystals phoretically assembled from a homogeneous distribution of bimaterial colloids—a TPM polymer colloidal sphere (3-methacryloxypropyl trimethoxysilane) with protruding hematite cube (inset)—under illumination by blue light [38]. (Bottom right) Swarm of starlings [48].*

and even exploit viscous drag. Hence, the rules governing swarming on the macroscale of flocks of birds or schools of fish are very different from those applying to the microscale of bacteria. Nevertheless, similar features appear on very distinct length scales.

A variety of models for active matter or agents has been developed to describe the aspect of interesting in sufficient detail. Examples are models for sperm [49] or *E. coli* bacteria [28] (see also references therein). From the theoretical side, rather generic models have been proposed, which lack details of real agents, but allow for a systematic study of active matter over a wide range of parameters. The prototype of a generic model is the active Brownian particle (ABP), a hard-sphere colloid, which actively moves in a prescribed direction, where the latter changes in a diffusive manner [2, 3]. This model has developed into the standard model to study the nonequilibrium statistical properties of active matter. A system of ABPs is a so called dry active system, because the ABPs are not embedded in a fluid, which is typically the case for biological and synthetic active matter. Fluid-mediated interactions (hydrodynamics) are captured by the so-called squirmer model for an active particle. Thereby, the squirmer is propelled by a prescribed flow velocity (slip velocity) on the colloid surface [50–54]. In the

hydrodynamic far field, the squirmer flow field is determined by the weakest decaying point multipoles, which are the source dipole and the force dipole flow field. Specifically, by the latter, the difference, e.g., between bacteria (pusher) and algae (puller) can be captured by a squirmer representation [52–54].
In this contribution, various specific aspects of active matter, compared to passive systems, will be discussed. First of all, active Brownian particles will be introduced and their properties be studied. Secondly, the low-Reynolds number hydrodynamics of microswimmers will be addressed. Specifically, the squirmer model is presented, and the difference of its collective behavior compared to ABPs is discussed.

# 2 Active Brownian particle (ABP)

The active Brownian particle captures essential aspects of a self-propelled object [2, 3, 35, 37, 41, 55–59]. It is typically represented as a repulsive spherical colloid (rigid body) propelled by a constant (external) force in the direction of its instantaneous orientation, which is changing in a diffusive manner. However, no hydrodynamic interactions are taken into account, an aspect to be kept in mind.

## 2.1 Equations of motion

The Langevin equations for the center-of-mass position $\boldsymbol{r}$ and the orientation $\boldsymbol{e}$ of an ABP are given by [10]

$$\dot{\boldsymbol{r}}(t) = \boldsymbol{v}(t) + \frac{1}{\gamma}\left(\boldsymbol{F}(t) + \boldsymbol{\Gamma}(t)\right), \tag{1}$$

$$\dot{\boldsymbol{e}}(t) = \boldsymbol{\xi}(t) \times \boldsymbol{e}(t), \tag{2}$$

where $\boldsymbol{v} = v_0\boldsymbol{e}$, with $\boldsymbol{e}$ a unit vector, is the propulsion velocity, $\boldsymbol{F}$ a force exerted on the particle, $\boldsymbol{\Gamma}$ and $\boldsymbol{\xi}$ are Gaussian and Markovian processes (white noise) with zero odd moments and the second moments

$$\langle \Gamma_\alpha(t)\Gamma_{\alpha'}(t')\rangle = 2\gamma k_B T\delta_{\alpha\alpha'}\delta(t-t'), \tag{3}$$

$$\langle \xi_\alpha(t)\xi_{\alpha'}(t')\rangle = (d-1)D_R\delta_{\alpha\alpha'}\delta(t-t'). \tag{4}$$

Here, $k_B$ is the Boltzmann constant, $T$ the temperature, $\gamma$ the translational friction coefficient, which is related to the translational diffusion coefficient $D_T$ via $D_T = k_BT/\gamma$, $D_R$ the rotational diffusion coefficient, $d$ the spatial dimension, and $\alpha, \alpha' \in \{x, y, z\}$. For a particle in a viscous fluid in three dimensions (3D), $\gamma = 6\pi\eta R$, with $\eta$ the viscosity and $R$ the particle radius, hence, $D_R$ and $D_T$ are related according to $D_T/D_RR^2 = 4/3$. However, in general, $D_R$ can be independent of $D_T$ and be of nonthermal origin, e.g., tumbling of bacteria. Equations (1) and (2) describe the solid-body translation and rotation, respectively. Thereby, we neglect the inertia terms, consistent with the fact that propulsion and motility on the nano- and microscale is typically governed by low-Reynolds number hydrodynamics (cf. Sec. 3) [2, 24]. The rotational motion (Eq. (2)) is independent of the colloid translation. As a particular result, the correlation function

$$\langle \boldsymbol{v}(t)\cdot\boldsymbol{v}(t')\rangle = v_0^2 e^{-(d-1)D_R|t-t'|} \tag{5}$$

is obtained ($d > 1$) [60–62]. In the above description, we consider the velocity $\boldsymbol{v}$ as an intrinsic property of the ABP. Alternatively, we can consider Eq. (1) only, with $\boldsymbol{v}$ as an external stochastic process with the exponential correlation (colored noise) of Eq. (5) [2, 41].
A general solution of Eqs. (1) and (2) is difficult to determine, even a stationary state solution, because of the violation of detailed balance [14] (cf. App. A). However, various aspects can be calculated directly, specifically for a zero force $\boldsymbol{F} = 0$.

## 2.2 Active Ornstein-Uhlenbeck particle (AOUP)

The propulsion direction $\boldsymbol{e}$, with Eq. (4), obeys the strict condition $|\boldsymbol{e}(t)| = 1$. By lifting this condition and considering the equation of motion for the propulsion velocity

$$\dot{\boldsymbol{v}}(t) = -\gamma_R \boldsymbol{v}(t) + \boldsymbol{\eta}(t), \tag{6}$$

a model is obtained, which is analytically easier tractable [2, 57, 63–67]. Here, the Cartesian velocity components are independent. The damping factor $\gamma_R$ is related to the rotational diffusion coefficient according to $\gamma_R = (d-1)D_R$, and $\boldsymbol{\eta}$ is a Gaussian and Markovian stochastic process with zero mean and the second moments

$$\langle \eta_\alpha(t)\eta_{\alpha'}(t')\rangle = \frac{2(d-1)}{d} v_0^2 D_R \delta_{\alpha\alpha'}\delta(t-t'). \tag{7}$$

The Langevin equations (6) with noise amplitudes ($v_0^2 D_R$), which are independent of the stochastic variables ($\boldsymbol{v}$), describe a process denoted as Ornstein-Uhlenbeck process [68]. Hence, an active particle obeying Eqs. (3) and (6) is denoted as active-Ornstein-Uhlenbeck particle (AOUP) [66]. Most importantly, an analytical solution and a stationary-state distribution function is obtained for a linear force $\boldsymbol{F}$ (harmonic potential) (cf. App. B) [67].

## 2.3 Mean square displacement

Integration of Eq. (1) in the force-free case ($\boldsymbol{F} = 0$) yields

$$\boldsymbol{r}(t) - \boldsymbol{r}(0) = \int_0^t \left( \boldsymbol{v}(t') + \frac{1}{\gamma}\boldsymbol{\Gamma}(t') \right) dt', \tag{8}$$

from which the mean square displacement $\Delta\boldsymbol{r}(t)^2 = \langle (\boldsymbol{r}(t) - \boldsymbol{r}(0))^2 \rangle$, with

$$\Delta\boldsymbol{r}^2 = \frac{6k_BT}{\gamma}t + \int_0^t \int_0^t \langle \boldsymbol{v}(t')\cdot\boldsymbol{v}(t'')\rangle \, dt'dt'' = 2dD_T t + \frac{2v_0^2}{\gamma_R^2}\left(\gamma_R t + e^{-\gamma_R t} - 1\right), \tag{9}$$

is obtained by insertion of the correlation function (5). Equation (9) turns, for small and large times, respectively, into

$$\Delta\boldsymbol{r}^2 = 2dD_T t + v_0^2 t^2, \quad \gamma_R t \ll 1; \qquad \Delta\boldsymbol{r}^2 = \left(2dD_T + \frac{2v_0^2}{\gamma_R}\right) t, \quad \gamma_R t \gg 1. \tag{10}$$

Hence, activity leads to a ballistic motion at short times, and a diffusive motion for $\gamma_R t \gg 1$ due to rotational diffusion of the propulsion direction, with the effective translational diffusion coefficient $D_{T,\text{eff}} = D_T + v_0^2/d(d-1)D_R$. The latter is much larger than $D_T$ for $v_0 \gg \sqrt{D_T D_R}$.

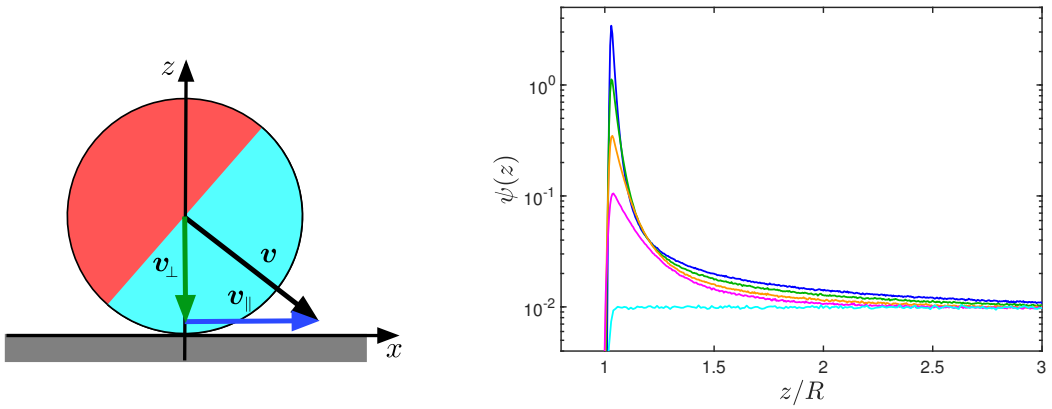


**Fig. 2:** *Surface accumulation of ABPs. (Left) Separation of the active velocity* $\boldsymbol{v} = v_0\boldsymbol{e}$ *parallel* ($\boldsymbol{v}_\parallel$) *and perpendicular* ($\boldsymbol{v}_\perp$) *to the surface. (Right) Probability distribution of an ABP in 3D confined between two parallel flat walls. The walls are located at* $z = 0$ *and* $z = 200R$*. The Péclet numbers are* $Pe = 0$, 5, 10, 20, *and* 40 *(bottom to top).*

Thus, activity leads to a drastically increased diffusive motion. The theoretical prediction of Eq. (9) has been confirmed experimentally, e.g., for phoretic Janus particles [55].
The activity of an ABP is usually characterized by the dimension less Péclet number

$$Pe = \frac{v_0}{2RD_R}. \tag{11}$$

Therefore, $D_{T,\text{eff}}/D_T$ is much larger than unity for $Pe \gg 1$. This corresponds to the regime, where activity dominates over thermal fluctuations.

## 2.4 Surface accumulation

Activity gives raise to various unusual and *a priori* unexpected effects. An example is the accumulation of ABPs even at purely repulsive walls [71]. The mechanism is illustrated in Fig. 2. The propulsion velocity ($\boldsymbol{v}$) of an ABP located at the wall can be separated in a component parallel ($\boldsymbol{v}_\parallel$) and normal ($\boldsymbol{v}_\perp$) to the wall. The parallel component leads to a translational motion of the center-of-mass parallel to the wall, since there is no friction between wall and ABP. The component normal to the wall pushes the swimmer toward the wall as long as $\boldsymbol{v}_\perp \cdot \boldsymbol{e}_z < 0$ ($\boldsymbol{e}_z$ is the unit vector along the $z$-axis), and the APB stays at the wall. Only after the change of the propulsion direction and for $\boldsymbol{v}_\perp \cdot \boldsymbol{e}_z > 0$, the particles leaves the wall again. This is different from thermal motion, where the velocity $\boldsymbol{v}_\perp$ is inverted instantaneously upon a collision with a (hard) wall. The appearing force onto the surface is calculated in Sec. 2.5. Figure 2 shows density profiles from simulations at various Péclet numbers for ABPs confined between to parallel walls in 3D, where the ABP-wall interaction is described by the Lennard-Jones potential (wall at $z = 0$)

$$U_{LJ}^w = \begin{cases} \epsilon\left[\left(\dfrac{R}{z}\right)^{48} - \left(\dfrac{R}{z}\right)^{24}\right] & , \; r < r_c \\ 0 & , \; r > r_c \end{cases}, \tag{12}$$

with $r_c = R\sqrt[6]{2}$. Hence, we use a soft, but steep potential. The different behavior compared to a thermal system is evident, as well as the density increase with increasing $Pe$. As a consequence, the distribution of active agents, e.g., in a convex container is dramatically affected

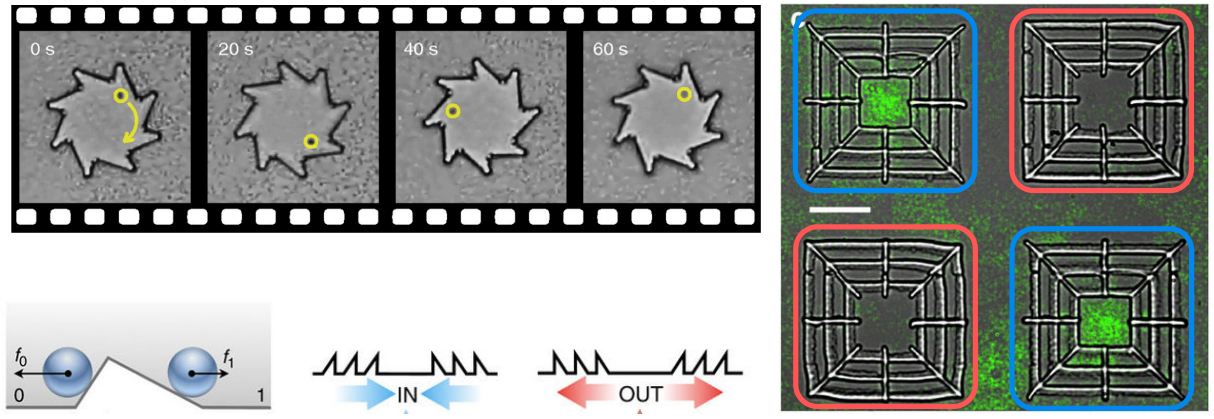


**Fig. 3:** *Rectification of bacteria motion. (Top left) Bacterial driven micromotor. A nano-fabricated asymmetric gear immersed in an active bath of motile* E. coli *cells rotates clockwise visualized by the yellow circle [69]. (Right) Steady-state distribution of colloidal particles in a bacterial bath exposed to an asymmetric square saw-tooth structure (scale bar* $20\mu m$*). There is a preferred transport in the direction of* $f_0$ *(bottom left), which leads to an accumulation of colloids inside (blue) or outside (red) of the squares [70].*

by the boundary shape in the limit, in which the container size is small compared to the active persistence length, $l_p = RPe$, the distance a particle travels before its orientation decorrelates. In particular, the particles are confined at the boundary and their steady-state distribution is proportional to the local curvature [72]. This effect can be exploited for rectification or trapping of active agents [73, 74]. Examples are provided in Fig. 3, where bacteria produce a spontaneous and unidirectional rotation of a nano-fabricated gear [69], or passive colloids are spatially organized by a suspension of swimming bacteria [70].

## 2.5 Active pressure

During the encounter with a wall (cf. Fig. 2), an ABP exerts a force on the wall due to propulsion [62]. The force can be estimated from Eq. (1). For simplicity, we consider a cubic volume, within ABPs are confined. The velocity of an ABP at a wall and in the direction of the wall normal $\boldsymbol{n}$ ($\boldsymbol{n}$ points outward of the volume) is zero, i.e., $\dot{\boldsymbol{r}} \cdot \boldsymbol{n} = 0$, which implies that $v_0 \boldsymbol{e} \cdot \boldsymbol{n} + \boldsymbol{F}^s \cdot \boldsymbol{n}/\gamma = 0$. Here, $\boldsymbol{F}^s$ is the force between the ABP and the wall, which we assume to be short ranged. Since $F_n = -\boldsymbol{F}^s \cdot \boldsymbol{n}$, we find

$$F_n(z_{max}) = \gamma v_0 \boldsymbol{e} \cdot \boldsymbol{n} \tag{13}$$

for the particle of Fig. 2 (left), where $z_{\max}$ is approximately equal to the $z$-position of the maximum in Fig. 2 (right). Defining surface stress (pressure) as force per area, $A$, Eq. (13) yields a the mechanical stress $\gamma v_0 e_z/A$ per particle. Extending the concept to a three-dimensional volume and taking into account $N$ ABPs in the volume $V$, the viral approach yields the more general expression for the pressure $3pV = -\sum_{i=1}^{N} \langle \boldsymbol{F}_i^s \cdot \boldsymbol{r}_i \rangle$ [62]. For a short-range surface interaction, the ABP $i$ is at a wall and $\boldsymbol{r}_i$ can be taken out of the sum, which leads to above stress (pressure) in the special case of single wall rather than six.
In systems with periodic boundary conditions, there are no confining walls. Here, as for any confined system, pressure can be calculated from the virial formulation exploiting the actual

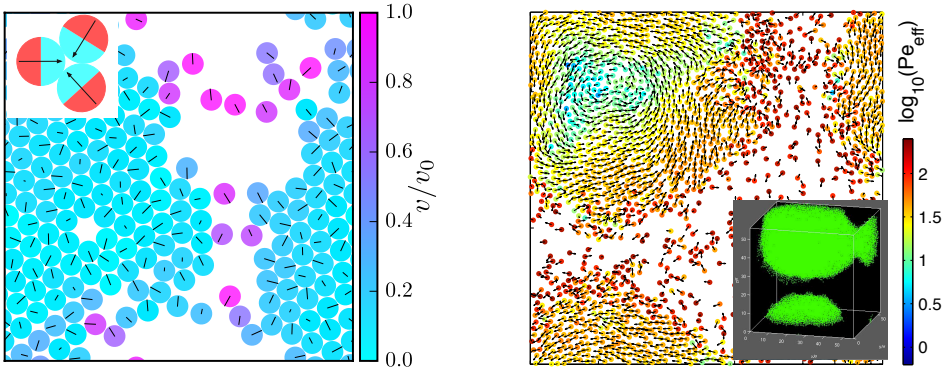


**Fig. 4:** *Motility-induced phase separation of ABPs. (Left) Two-dimensional well-ordered cluster in contact with a gas of ABPs. The inset illustrates the blockage of three particles. (Right) Highly dynamic cluster in three dimensions in contact with a gas of ABPs. In inset shows the three-dimensional structure.*

positions and velocities of the ABPs. This approach leads to the pressure [62]

$$3pV = 3Nk_BT + 3Nk_BT\frac{v_0^2}{6D_TD_R} + \sum_{i=1}^{N}\langle \boldsymbol{F}_i^s\cdot\boldsymbol{e}_i\rangle + \frac{1}{2}\sum_{i=1}^{N}\sum_{j=1}^{N}{}'\langle \boldsymbol{F}_{ij}\cdot(\boldsymbol{r}_i-\boldsymbol{r}_j)\rangle\,. \qquad (14)$$

The first term on the right hand side is the ideal gas contribution due to the Brownian motion of the ABP center of mass. The second term is the swim pressure, which is proportional to the square of the propulsion velocity [75]. The third terms captures corrections due to interactions with the walls; the term vanishes for infinite system sizes. Finally, the last term accounts for interparticle interactions. Compared to passive systems, the second and third term appear additionally.

Active systems are out of equilibrium and equilibrium statistical mechanics and thermodynamics cannot strictly be applied in their description. This is, e.g., reflected by the fact that temperature is ill defined in active systems [67], hence, there is no equation of state, in general, relating properties such as density and temperature with other thermodynamic bulk properties [76]. As shown above, there is an equation of state for the pressure of spherical ABPs confined in an orthorhombic volume. However, as discussed in Ref. [76], no such equation exists for an active fluid in general, since small orientation-dependent interactions (whether wall-particle or particle-particle) immediately destroy the equation of state. Such interactions are typically present in every experimental system. Yet, the mechanical pressure is well defined and can be calculated.

## 2.6 Motility-induced phase separation (MIPS)

The mechanism responsible for accumulation of ABPs at walls (Sec. 2.4) leads also to novel bulk phenomena. In dilute systems, clusters emerge and a motility-induced phase separation [3], as illustrated in Fig. 1. When two or three particles collide, they block each other due to their persistent motion as sketched in Fig. 4 (left). The particular cluster would resolves after a time $t \sim 1/\gamma_R$ due to the rotational diffusion of the orientation $\boldsymbol{e}$. Interactions and collisions with other particles are controlled by the density and velocity $v_0$. Hence, if other particles collide before the original cluster resolved, the cluster grows. At higher concentrations, a phase

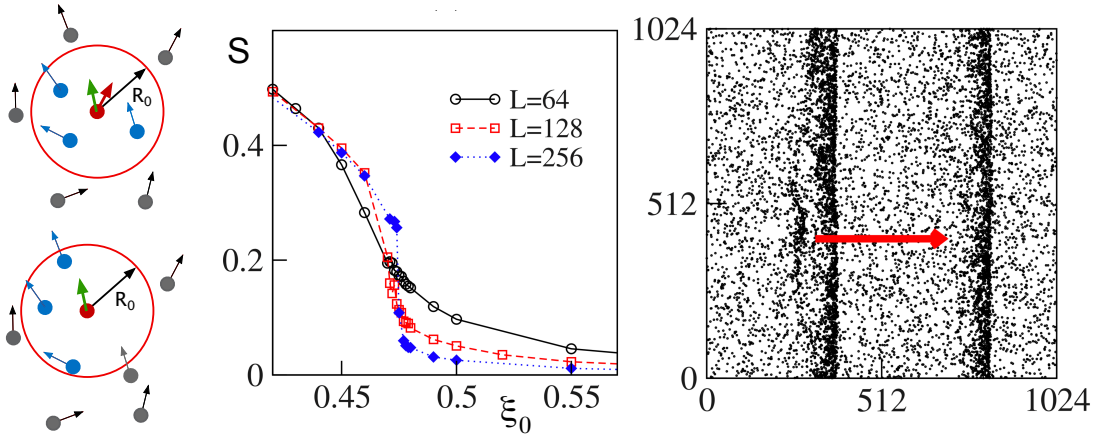


**Fig. 5:** *(Left) Illustration of the Vicsek dynamics. The red central particle with original orientation (red) aligns with neighbours (green) inside the circle of radius $R_0$ (red) (top), and then moves along its heading direction (bottom). (Middle) Magnitude $S = |\boldsymbol{S}|$ of the order parameter as function of noise strength $\xi_0$ for various system sizes $L$. (Right) Snapshot in the ordered phase. Points represent the individual particles and the red arrow indicates the global direction of motion. Periodic boundary conditions are applied for the 2D system. The simulation parameters can be found in Ref. [77].*

transition in a high-density and a low density phase can appear, as depicted in Fig. 4. Thereby, the structure of the high density phase depends on the spatial dimension. In 2D, this phase is typically well ordered in a hexagonal fashion [3, 35], whereas in 3D, the high-density phase is rather mobile [39].

## 2.7 Collective motion—the Vicsek model

The three-dimensional APB system of Sec. 2.6 (Fig. 4) exhibits collective motion without any alignment rule between neighbors. Collective motion is often studied by implementing an alignment rule for spherical particles, or emerges naturally due to the anisotropy of the active particles, e.g., rods [78]. A prototypical example for a system with an explicit alignment rule is the Vicsek model [14, 79, 80].

The translational motion of a force free ($\boldsymbol{F} = 0$) particle within the Vicsek model is given by Eq. (1), however the thermal noise is neglected, i.e, $\boldsymbol{\Gamma} = 0$. Particles are assumed to align their direction of motion with their local neighbors. Hence, the orientation $\boldsymbol{e}_i$ of particle $i$ depends on the average direction of all particles (including particle $i$) in a spherical neighborhood of radius $R_0$ centered at $\boldsymbol{r}_i$ (cf. Fig. 5). In fact, alignment within a neighborhood is almost perfect, its only perturbed by thermal-type white noise. For simplicity, we focus on 2D systems, where the direction of motion is determined by the angle $\theta_i$, with $\boldsymbol{e}_i = (\cos\theta_i, \sin\theta_i)^T$. The angle itself changes in time according to

$$\theta_i = \mathrm{Arg}\left(\sum_j \Theta(R_0 - |\boldsymbol{r}_i(t) - \boldsymbol{r}_j(t)|)\boldsymbol{e}_j(t)\right) + \xi_0 \Delta\xi_i(t). \tag{15}$$

The argument Arg yields the angle between the effective vector $\sum_j \Theta(R_0 - |\boldsymbol{r}_i(t) - \boldsymbol{r}_j(t)|)\boldsymbol{e}_j(t)$ and an arbitrary direction. Here, $\Theta(x)$ is the Heaviside step function, $\Delta\xi_i$ white noise with the correlation function $\langle \Delta\xi_i(t)\Delta\xi_j(t)\rangle = 2\delta_{ij}$, and $\xi_0$ is the noise amplitude.

Simulations show that the Vicsek model exhibits a transition from disordered to ordered collective motion. The degree of ordering depends on the parameter $\xi_0$. A measure for the degree of alignment is the order parameter $\boldsymbol{S}(t) = \sum_{i=1}^{N} \boldsymbol{e}_i(t)/N$, where $N$ is the number of active particles. Figure 5 (middle) displays the dependence of the order parameter on the noise strength for various system sizes. For large systems and below a certain $\xi_0$, a first order phase transition appears from a disordered to an ordered collective dynamic state [77]. The emerging sharp bands are illustrated in Fig. 5 (right).

# 3 Life at low Reynolds numbers

## 3.1 Hydrodynamics

Typically, the dynamics of the incompressible (isothermal) fluid flow field surrounding a microswimmer is described by the Navier-Stokes equations

$$\rho\left(\frac{\partial}{\partial t}\boldsymbol{v} + (\boldsymbol{v}\cdot\nabla)\,\boldsymbol{v}\right) = -\nabla p + \eta\nabla^2\boldsymbol{v} + \boldsymbol{f}\,, \qquad \nabla\cdot\boldsymbol{v} = 0, \tag{16}$$

where $\boldsymbol{v}(\boldsymbol{r},t)$, $p(\boldsymbol{r},t)$, and $\boldsymbol{f}(\boldsymbol{r},t)$ are the velocity, pressure, and volume-force-density fields, respectively. At small Reynolds numbers $Re = \rho u L/\eta \ll 1$, where $\rho$ is the fluid mass density, $u$ the characteristic velocity, $L$ the size of the micoswimmer, and $\eta$ the fluid viscosity, the inertia terms on the left-hand side of Eq. (16) can be neglected, and the equations reduce to the Stokes or creeping flow equations

$$\nabla p(\boldsymbol{r}) - \eta\nabla^2\boldsymbol{v}(\boldsymbol{r}) = \boldsymbol{f}(\boldsymbol{r})\,, \qquad \nabla\cdot\boldsymbol{v} = 0. \tag{17}$$

For illustration, the Reynolds number in water of a swimmer of length $L = 10\ \mu$m, a velocity of $u = 50\mu$m/s, and the kinematic viscosity $\nu = \eta/\rho = 10^{-6}$m$^2$/s is $Re \approx 10^{-3}$. The Stokes equation (17) is linear and time independent. The consequences of this intrinsic symmetry under time reversal for microswimmers undergoing periodic shape changes was first expressed in Ref. [43] by Purcell, and is now know as "scallop theorem", which can be stated as: if the shape changes displayed by a swimmer are identical when viewed in reverse order, it will generate an oscillatory, but no directed motion [2,24,43,81]. Thus, just by opening and closing its two shells, a mussel (scallop) cannot move forward at $Re \ll 1$. Microswimmers developed various strategies to beat the scallop theorem. Aside from many (elastic) degrees of freedom, they use specific propulsion mechanisms—bacteria such es *E. coli* are propelled by rotating helical flagella bundles, sperm use sinusoidal bending waves propagating from head to tail, and algae, e.g., *Chlamydomonas* uses an non-reciprocal stroke pattern.

## 3.2 Solution of Stokes equation

The linear Stokes equations (17) are easily solved analytically for an unbounded fluid. The respective velocity field is

$$\boldsymbol{v}(\boldsymbol{r}) = \int \mathbf{Q}(\boldsymbol{r}-\boldsymbol{r}')\boldsymbol{f}(\boldsymbol{r}')\,d^3r'\,, \quad Q_{\alpha\alpha'}(\boldsymbol{r}) = \frac{1}{8\pi\eta r}\left[\delta_{\alpha\alpha'} + \frac{r_\alpha r_{\alpha'}}{r^2}\right], \tag{18}$$

where $\mathbf{Q}(\boldsymbol{r})$ is the well-know Oseen tensor, with the Cartesian components $Q_{\alpha\alpha'}$ ($\alpha,\alpha' \in \{x,y,z\}$) and $r = |\boldsymbol{r}|$ [82, 83]. The Oseen tensor, also denoted as Stokeslet, shows that hydrodynamic interactions are long ranged, with a $1/r$ decay like the Coulomb potential, and it is

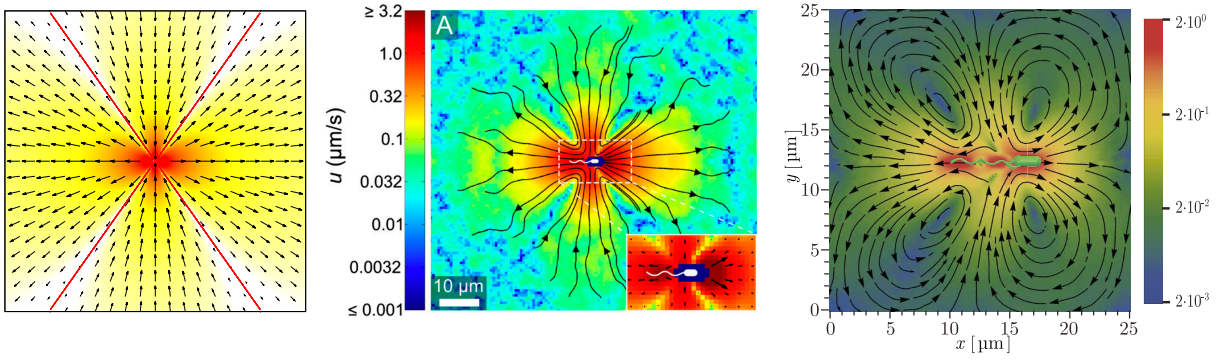


**Fig. 6:** *(Left) Flow lines of a hydrodynamic dipole oriented horizontally, Eq. (20) [2]. The separatrices between the inflow and outflow regions are shown by thick red lines. Flow field of a* E. coli *bacterium from (Middle) experiment [84] and (Right) simulations [28]. In simulations, a system with periodic boundary conditions is considered, which yields closed flow lines in contrast to the flow lines of the experimental bulk system. The logarithmic color scheme (right) indicates the magnitude of the flow speed scaled by the bacterial swimming velocity.*

anisotropic due to the incompressibility of the fluid. The Oseen tensor is the Green's function of the Stokes equation (17), which is evident, when the point force $\boldsymbol{f}(\boldsymbol{r}) = f_0\delta(\boldsymbol{r})\boldsymbol{e}$ in the direction $\boldsymbol{e}$ ($|\boldsymbol{e}| = 1$) is inserted. Then, Eq. (18) yields

$$\boldsymbol{v}(\boldsymbol{r}) = \frac{f_0}{8\pi\eta r}\left[\boldsymbol{e} + \frac{(\boldsymbol{r}\cdot\boldsymbol{e})\boldsymbol{r}}{r^2}\right]. \tag{19}$$

The magnitude of the flow field is evidently twice larger in the force direction than perpendicular to it.

## 3.3 Force dipole

Most swimmers move autonomously, with no external force or torque applied, and hence the total interaction force/torque of the swimmer on the fluid, and *vice versa*, vanishes. In the simplest case, which actually applies to many microswimmers like bacteria, spermatozoa, or algae, the far-field hydrodynamics (at distances from the swimmer much larger than its size) can well be described by a force dipole [24, 85]. This has been confirmed experimentally for *E. coli* [84, 86] and in simulations [28]. The flow field of *Chlamydomonas* is well reproduced by three Stokeslets [86].

Mathematically, the flow field $\boldsymbol{v}_d(\boldsymbol{r}-\boldsymbol{r}_0)$ of a hydrodynamic force dipole located at $\boldsymbol{r}_0$ follows by a superposition of two Stokeslets (18) with opposite forces $\boldsymbol{f}_0 = \pm f_0\boldsymbol{e}$ of equal magnitude at $\boldsymbol{r}_0 \pm \boldsymbol{l}/2$, where $\boldsymbol{l} = l\boldsymbol{e}$. Taylor expansion to leading order in $|\boldsymbol{l}|/|\boldsymbol{r}-\boldsymbol{r}_0|$ yields

$$\boldsymbol{v}_d(\boldsymbol{r}) = \frac{P}{8\pi\eta r^3}\left[-1 + 3\frac{(\boldsymbol{r}\cdot\boldsymbol{e})^2}{r^2}\right]\boldsymbol{r}, \tag{20}$$

where $P = \pm f_0 l$ is the dipole strength. Note that the flow field of a force dipole decays as $1/r^2$ from the center of the dipole, faster than the force monopole (Stokeslet) (18). The flow lines of a hydrodynamic dipole oriented vertically ($x$-direction) are displayed in Fig. 6. There are two inflow and two outflow regions in the $xy$-projection, which are separated by the separatrices $y = \pm\sqrt{2}x$. In three dimensions, the outflow region is a cone.

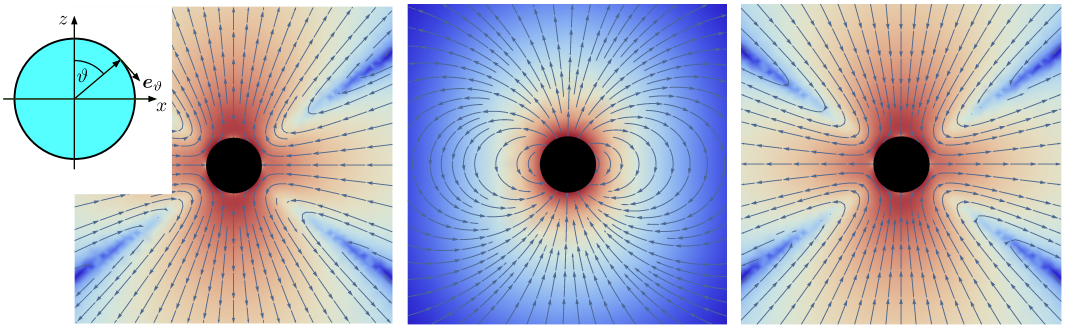


**Fig. 7:** *Flow streamlines of isolated squirmers in the laboratory reference frame for (Left) a pusher ($\beta < 0$), (Middle) a neutral squirmer ($\beta = 0$), and (Right) a puller ($\beta > 0$). The inset indicates the definition of the angle $\vartheta$ and the tangential vector $\boldsymbol{e}_\vartheta$ in the squirmer-fixed reference frame.*

Two classes of dipole swimmers can be distinguished, A swimmer with its "motor" in the back, and a passive body dragging along the surrounding fluid in front, creates a "pusher" flow field (cf. Fig. 6 (left)). Similarly, a swimmer with its "motor" in front, and the passive body dragging along the fluid behind, develops a "puller" flow field. The flow fields of pushers and pullers look similarly, but with opposite flow directions. This has important consequences for the interactions between swimmers and of swimmers with walls.
The flow field of an *E. coli* bacterium obtained from experiment [84] and simulations [28] is presented in Fig. 6. In both cases, the far field is well described the force dipole field of Eq. (20) [28]. However, there is also a distinct near field determined by the shape of the bacterium.

## 3.4 Squirmer—a model hydrodynamic microswimmer

A prototype of a swimmer capturing hydrodynamics is the squirmer, which was introduced by Lighthill [50] and revised by Blake [51]. Originally, it was intended as a model for ciliated microswimmers such as Paramecia. Nowadays, it is considered as a generic model for a broad class of microswimmers, ranging from diffusiophoretic particles [3, 55, 87, 88] to biological cells, and has been applied to study collective effects in bulk [52, 53, 89–93], at surfaces [53, 94, 95], and in narrow slits [96, 97]. In its simplest form, a squirmer is represented as a spherical rigid colloid with a prescribed surface velocity [50, 51, 90, 97]. Restricting the surface (slip) velocity to be tangential, the spherical squirmer is typically characterized by two modes accounting for its swimming velocity ($B_1$) and its force dipole ($B_2$). Explicitly, the slip velocity is then given by (cf. Fig. 7) [2, 53, 90, 97]

$$\boldsymbol{v}_{sq} = (B_1 \sin\vartheta + B_2 \sin\vartheta\cos\vartheta)\boldsymbol{e}_\vartheta = B_1(\sin\vartheta + \beta\sin\vartheta\cos\vartheta)\boldsymbol{e}_\vartheta. \tag{21}$$

The parameter $B_1 = 2v_0/3$ is related to the swimming velocity, $v_0$, and $\beta = B_2/B_1$ accounts of the force dipole. Higher order term can easily be taken into account [2,53]. By the term with $B_2$ (or $\beta$), we can distinguish between pushers ($\beta < 0$), pullers ($\beta > 0$), and neutral squirmers ($\beta = 0$), corresponding, e.g., to *E. coli*, *Chlamydomonas*, or *Volvox*, respectively.
The far field of a squirmer is well described by the flow fields of a force dipole (FD), a source dipole (SD), and a source quadrupole (SQ)

$$\boldsymbol{v}(\boldsymbol{r}) = \kappa^{FD}\boldsymbol{v}^{FD}(\boldsymbol{r}) + \kappa^{SD}\boldsymbol{v}^{SD}(\boldsymbol{r}) + \kappa^{SQ}\boldsymbol{v}^{SQ}(\boldsymbol{r}) + \mathcal{O}(r^{-5}), \tag{22}$$

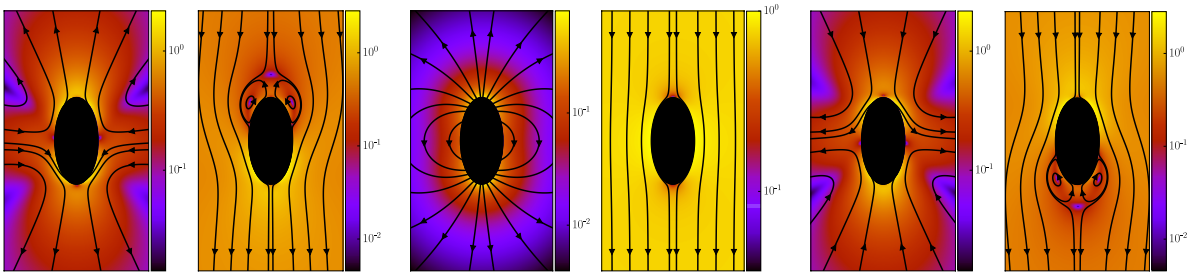

**Fig. 8:** *Flow field of a spheroidal squirmer with the aspect ration two. For each of the three pairs, the left image is the flow field in the laboratory reference frame and the right image in the body-fixed frame. (Left) Pusher with $\beta = -3$, (Middle) neutral squirmer ($\beta = 0$), and (Right) puller with $\beta = 3$. The magnitude of the velocity field is color coded logarithmically.*

where

$$\boldsymbol{v}^{FD}(\boldsymbol{r}) = \frac{\boldsymbol{r}}{r^3}\left(\frac{3z^2}{r^2} - 1\right), \tag{23}$$

$$\boldsymbol{v}^{SD}(\boldsymbol{r}) = \frac{1}{r^3}\left(-\boldsymbol{e}_z + \frac{3z\boldsymbol{r}}{r^2}\right), \tag{24}$$

$$\boldsymbol{v}^{SQ}(\boldsymbol{r}) = \frac{3}{r^4}\left(\frac{5z^2\boldsymbol{r}}{r^3} - \frac{2z\boldsymbol{e}_z + \boldsymbol{r}}{r}\right), \tag{25}$$

which decay like $r^{-2}$, $r^{-3}$, and $r^{-4}$ [98], respectively, and $\kappa^{FD} = P/8\pi\eta$, $\kappa^{SD} = -v_0R^3/2$, and $\kappa^{SQ} = PR^3/8\pi\eta$. Note that in Eqs. (23)-(25) the swimming direction $\boldsymbol{e}$ points along the positive $z$ axis, and $\boldsymbol{e}_z$ is the unit vector along that axis. Figure 7 depicts flow fields of the various kinds of microswimmers. In the far field, the flow fields of pushers and pullers are given by the force-diploe field (23) (or Eq.(20)).
The assumption of a spherical shape is adequate for swimmers like, e.g., *Volvox*, however, the shapes of other microswimmers (*E. coli, Chlamydomonas*, *Paramecium*) are nonspherical. Here, an extension of the squirmer concept to spheroidal objects has been proposed [97, 99]. Figure 8 depicts flow fields of a spheroidal squirmer with the aspect ratio of two for the various kinds of dipolar terms (Eqs. (23), (24)) in the laboratory and body-fixed reference frame. The near-field modifications by the finite-size swimmer is clearly visible in comparison with Fig. 6 (left). Moreover, pusher and puller exhibit a stagnation point in front or back, respectively, in the body-fixed reference frame.

## 3.5 Squirmer cooperative locomotion

Hydrodynamic interactions substantially affect the properties of active particles. An example is the cooperative motion of two spheroidal squirmers confined in a thin slit by two no-slip walls (cf. Fig. 9). Initially, the squirmer's surface-to-surface distance is $d_s = 3.5a$ and the angle between their swim directions $\theta_0 = 3\pi/8$. Due to the setup, the squirmers initially approach each other and collide at $tv_0/\sigma \approx 0.5$ (cf. Fig 9 (right)). The (persistence) Péclet number $Pe = v_0/(2D_R^{\perp}\sigma) \approx 60$ is sufficiently large, such that the squirmer orientation has hardly changed before collision. When the neutral squirmers collide, they initially align parallel ($\cos\theta \approx 1$ at $tv_0/\sigma \approx 1$ in Fig. 9), but their trajectories start to diverge immediately thereafter. Pushers remain parallel for an extended time window, which is expected as pushers

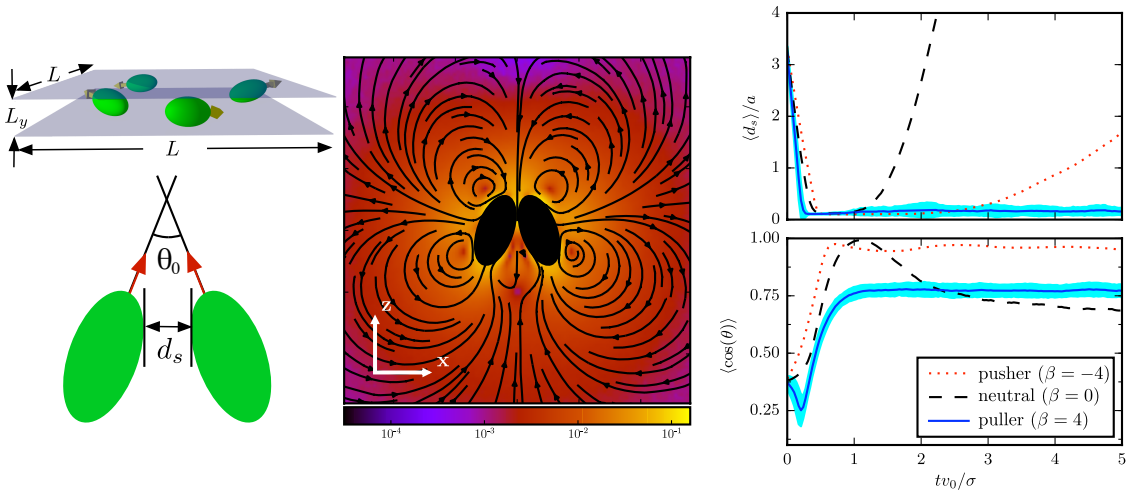


**Fig. 9:** *(Left) Definition of the geometry of the confined squirmers, their orientation, and distance. (Middle) Flow streamlines of two pullers swimming cooperatively (laboratory reference frame). The magnitude of the velocity field is color coded logarithmically. (Right) Average surface-to-surface distance $d_s$ and orientation of squirmers, where $\cos(\theta) = \boldsymbol{e}_1 \cdot \boldsymbol{e}_2$, as function of time. The solid blue, dashed black, and dotted red lines correspond to pullers ($\beta = 4$), neutral squirmers, and pushers ($\beta = 4$). The standard deviation of the blue line is indicated by the cyan shaded region [54].*

are known to attract each other [89], but at $tv_0/\sigma \approx 3$ (cf. Fig. 9) their trajectories diverge as well. This is probably due to noise, since we observe several realizations where pushers remain parallel for an extended time. Interestingly, pullers, which are known to repel each other when swimming in parallel [89] (cf. Fig. 7 for the flow field), swim cooperatively and reach a stable orientation with $\langle \cos(\theta) \rangle \approx 0.77$ shortly after they collided ($tv_0/\sigma \approx 1$). Thereby, their cooperative swimming velocity is about $0.8v_0$. The flow field of this stable state, determined by MPC simulations, is shown in Fig. 9 (middle). Note that the velocity field in the swimming plane is left-right symmetric, and that there is a stagnation point in the center behind the swimmers. This point actually corresponds to a line normal to the walls [97]. In contrast, in Ref. [90] a cooperative swimming mode for spherical squirmers has been observed (see Fig. 22(c) of Ref. [90]). However, this cooperative swimming—termed pair-swimming by the authors—is unstable to perturbations that displace one swimmer out of the swimming plane [90]. Since our simulations and those of Ref. [89] include thermal fluctuations, we consequently do not observe the cooperative swimming mode of Ref. [90].
Hence, the stable close-by cooperative swimming of pullers is governed by the squirmer anisotropy, by the hydrodynamic interactions between them and, importantly, between pullers and confining surfaces.

## 3.6 Squirmer cluster formation

As discussed in Sec. 2.6, activity leads to MIPS in ABPs systems. Detailed studies reveal substantial changes in the phase behavior of active particles in the presence of hydrodynamic interactions [96,100–103]. Hydrodynamic simulation studies of disks (2D system) [100], where MIPS is most pronounced for APBs, show no evidence for a bulk phase separation. The qualitative different behavior is attributed to an emergent faster decorrelation of the squirmers swim-

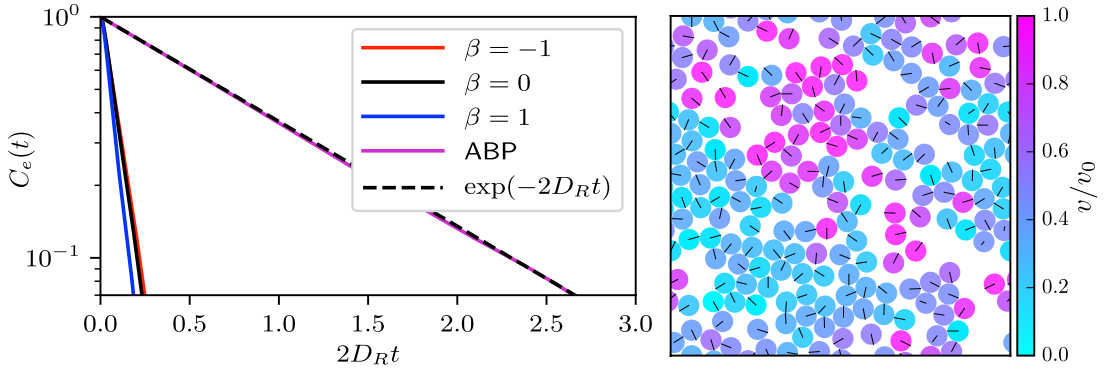


**Fig. 10:** *(Left) Time dependence of the orientation correlation function $C_e(t)$ for a system of spherical squirmers and active Brownian particles. The dashed line indicates the exponential decay with the rotational diffusion coefficient $D_R$. (Right) Snapshot of a configuration of squirmers. The two-dimensional packing fraction is $\phi^{2D} = 0.6$ and the Péclet number $P_e = 115$.*

ming direction due to HIs compared to the Brownian rotational motion of ABPs. Similar results have been found for spherical squirmers confined in a narrow slit [104]. Figure 10 displays a snapshot of the structure of a system of neutral squirmers. Neither large clusters nor a pronounced order is present for neutral squirmers (compare with Fig. 4). Similarly, no MIPS is observed for pusher and pullers. In addition, Fig. 10 shows the time dependence of the orientation correlation function of the propulsion direction $C_e(t) = \sum_{i=1}^{N_s} \langle \boldsymbol{e}_i(t) \cdot \boldsymbol{e}_i(0) \rangle / N_s$, where $N_s$ is the number of squirmers in the system. The significant faster decay of the correlation function compared to ABPs is evident, with little difference between pushers, pullers, and neutral squirmers. Note that the correlation function of an individual squirmer decays similarly to the correlation function of an APB. Hence, the enhanced decay is a consequence of inter-squirmer interactions.

Structure formation is decisively affected by the shape of a microswimmer (squirmer). On the one hand, it is expected that an elongated shape enhances parallel alignment due to steric interactions, an effect already present for elongated ABPs [78, 105]. On the other hand, hydrodynamic interactions prevent stable aligned states, at least for pusher and neutral squirmers. The question is how hydrodynamics ultimately affects MIPS of elongated squirmers keeping in mind that hydrodynamics suppresses MIPS for spherical squirmers. Our computer simulations show that hydrodynamics enhances cluster formation for spheroidal squirmers. This is illustrated in Fig. 11. At the same Péclet number, $Pe = 12$, spheroids with the aspect ratio three exhibit evidently a highly compact and large-scale aggregate in contrast to the gas-like spherical system. Interestingly, hydrodynamic interactions enhance cluster formation, as shown in Fig. 11 (right). ABPs show the least tendency to form clusters for $Pe = 12$, followed by pushers and neutral squirmers; pullers show the highest tendency for cluster formation, already at rather low densities.

# 4 Conclusions

Active matter exhibits a spectrum of unusual and fascinating phenomena, and offers many promising avenues for creating novel materials with tunable properties. Most remarkably is the intriguing collective behavior with emerging large-scale turbulence-like flow, or motility-

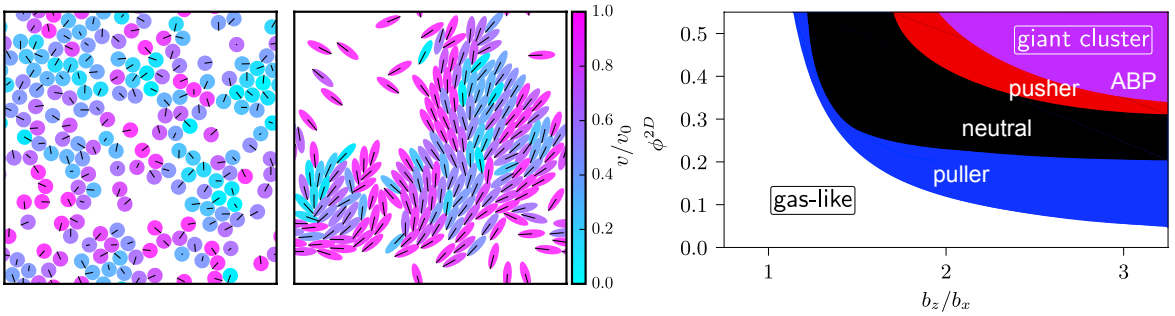


**Fig. 11:** *(Left) Snapshots of spherical and spheroidal (aspect ratio three) squirmer configurations. (Right) Density-aspect ratio state diagram for ABPs, pullers ($\beta = 1$), neutral squirmers ($\beta = 0$), and pushers ($\beta = 1$). Here, $b_z$ denotes the long and $b_x$ the short axis of the spheroid. The density is $\phi^{2D} = 0.6$ and $P_e = 12$.*

induced phase separation. Here, active Brownian particles are an excellent model system to unravel the underlying generic principles of out-of-equilibrium systems. Remarkably, hydrodynamic interactions are essential for active matter, specifically biological microswimmers, and are able to completely alter the steady-state behavior of interacting motile particles. Hydrodynamic interactions are not only fundamental for the propulsion of microswimmers (see contribution **E4**), but also determine their behavior next to surfaces as well as the emergent collective dynamics and structures. Hydrodynamic interactions imply a very rich dynamics, which depends on the detailed swimming mechanism. We are only at the beginning of our strive to elucidate the properties of active matter. Specifically, the design of novel synthetic active agents and the control of existing (mostly biological) agents requires intensive studies in the future, both from the theoretical and the experimental side.

# Appendices

## A Fokker-Planck equation of ABP

Equivalently to the Langevin equations (1) and (2), the dynamics of an ABP is described by the Fokker-Planck equation for the distribution function $\psi(\boldsymbol{r}, \boldsymbol{e}, t)$,

$$\frac{\partial \psi}{\partial t} = -\frac{\partial}{\partial \boldsymbol{r}} \left( \left[ v_0 \boldsymbol{e} + \frac{1}{\gamma} \boldsymbol{F} \right] \psi \right) + D_T \frac{\partial^2}{\partial \boldsymbol{r}^2} \psi + D_R \frac{\partial^2}{\partial \boldsymbol{e}^2} \psi. \tag{26}$$

Here, $\partial^2/\partial \boldsymbol{e}^2$ is the Laplace operator in polar (2D) or spherical (3D) coordinates. There is typically no simple way to find a stationary-state ($\partial\psi/\partial t = 0$) solution of this equation, because detailed balance is violated [14]. According to Refs. [68, 106], the stationary state distribution function, or the generalized potential [68], is required to examine detailed balance. A necessary and sufficient condition for the existence of a potential for Eq. (26) is $v_0 \partial e_\alpha / \partial e_{\alpha'} = 0$, $\forall \alpha, \alpha'$, (natural boundary conditions are assumed), which is only satisfied for $v_0 = 0$. Note that there is no drift term related to the orientation $\boldsymbol{e}$. Hence, there is in general no potential and a stationary-state solution is difficult to obtain [68].

# B Fokker-Planck equation of AOUP

The Fokker-Planck equation for the distribution function $\psi(\boldsymbol{r}, \boldsymbol{v}, t)$ of the AOUP dynamics (6) reads [67]

$$\frac{\partial}{\partial t}\psi = -\frac{\partial}{\partial \boldsymbol{r}}\left(\left[\boldsymbol{v} + \frac{1}{\gamma}\boldsymbol{F}\right]\psi\right) + 2D_R\frac{\partial}{\partial \boldsymbol{v}}\left(\boldsymbol{v}\psi\right) + D_T\frac{\partial^2}{\partial \boldsymbol{r}^2}\psi + \frac{2D_R v_0^2}{3}\frac{\partial^2}{\partial \boldsymbol{v}^2}\psi. \tag{27}$$

Due to the Gaussian nature of the stochastic processes, and the fact that a Gaussian is determined by its first and second moment, the full time-dependent solution of Eq. (27) can be obtained for the special case of a harmonic potential, i.e., a linear force [67, 68].

# References


[1] M. E. Cates and F. C. MacKintosh, Soft Matter **7**, 3050 (2011).

[2] J. Elgeti, R. G. Winkler, and G. Gompper, Rep. Prog. Phys. **78**, 056601 (2015).

[3] C. Bechinger, R. Di Leonardo, H. Löwen, C. Reichhardt, G. Volpe, and G. Volpe, Rev. Mod. Phys. **88**, 045006 (2016).

[4] D. Needleman and Z. Dogic, Nat. Rev. Mater. **2**, 201748 (2017).

[5] S. Ramaswamy, J. Stat. Mech. Theor. Exp. **2017**, 054002 (2017).

[6] A. S. Mikhailov and R. Kapral, Proc. Natl. Acad. Sci. USA **112**, E3639 (2015).

[7] R. Kapral and A. S. Mikhailov, Physica D **318-319**, 100 (2016).

[8] H. S. Muddana, S. Sengupta, T. E. Mallouk, A. Sen, and P. J. Butler, J. Am. Chem. Soc. **132**, 2110 (2010).

[9] K. K. Dey, S. Das, M. F. Poyton, S. Sengupta, P. J. Butler, P. S. Cremer, and A. Sen, ACS Nano **8**, 11941 (2014).

[10] R. G. Winkler, J. Elgeti, and G. Gompper, J. Phys. Soc. Jpn. **86**, 101014 (2017).

[11] Y. Harada, A. Noguchi, A. Kishino, and T. Yanagida, Nature **326**, 805 (1987).

[12] V. Schaller, C. Weber, C. Semmrich, E. Frey, and A. R. Bausch, Nature **467**, 73 (2010).

[13] F. Jülicher, K. Kruse, J. Prost, and J.-F. Joanny, Phys. Rep. **449**, 3 (2007).

[14] M. C. Marchetti, J. F. Joanny, S. Ramaswamy, T. B. Liverpool, J. Prost, M. Rao, and R. A. Simha, Rev. Mod. Phys. **85**, 1143 (2013).

[15] J. Prost, F. Jülicher, and J.-F. Joanny, Nat. Phys. **11**, 111 (2015).

[16] A. Cordoba, J. D. Schieber, and T. Indei, RSC Adv. **4**, 17935 (2014).

[17] Y. Sumino, K. H. Nagai, Y. Shitaka, D. Tanaka, K. Yoshikawa, H. Chate, and K. Oiwa, Nature **483**, 448 (2012).

[18] C. P. Brangwynne, G. H. Koenderink, F. C. MacKintosh, and D. A. Weitz, J. Cell. Biol. **183**, 583 (2008).

[19] C. P. Brangwynne, G. H. Koenderink, F. C. MacKintosh, and D. A. Weitz, Phys. Rev. Lett. **100**, 118104 (2008).

[20] C. A. Weber, R. Suzuki, V. Schaller, I. S. Aranson, A. R. Bausch, and E. Frey, Proc. Natl. Acad. Sci. USA **112**, 10703 (2015).

[21] S. C. Weber, A. J. Spakowitz, and J. A. Theriot, Proc. Natl. Acad. Sci. USA **109**, 7338 (2012).

[22] A. Javer, Z. Long, E. Nugent, M. Grisi, K. Siriwatwetchakul, K. D. Dorfman, P. Cicuta, and M. Cosentino Lagomarsino, Nat. Commun. **4**, 3003 (2013).

[23] A. Zidovska, D. A. Weitz, and T. J. Mitchison, Proc. Natl. Acad. Sci. USA **110**, 15555 (2013).

[24] E. Lauga and T. R. Powers, Rep. Prog. Phys. **72**, 096601 (2009).

[25] H. C. Berg, *E. Coli in Motion*, Biological and Medical Physics Series (Springer, New York, 2004).

[26] C. Brennen and H. Winet, Ann. Rev. Fluid Mech. **9**, 339 (1977).

[27] S. Y. Reigh, R. G. Winkler, and G. Gompper, Soft Matter **8**, 4363 (2012).

[28] J. Hu, M. Yang, G. Gompper, and R. G. Winkler, Soft Matter **11**, 7843 (2015).

[29] R. M. Macnab, Proc. Natl. Acad. Sci. USA **74**, 221 (1977).

[30] L. Turner, W. S. Ryu, and H. C. Berg, J. Bacteriol. **182**(10), 2793 (2000).

[31] D. B. Kearns, Nat. Rev. Microbiol. **8**, 634 (2010).

[32] H. H. Wensink, J. Dunkel, S. Heidenreich, K. Drescher, R. E. Goldstein, H. Löwen, and J. M. Yeomans, Proc. Natl. Acad. Sci. USA **109**, 14308 (2012).

[33] G. Popkin, Nature **529**, 16 (2016).

[34] F. Wong, K. K. Dey, and A. Sen, Annu. Rev. Mater. Res. **46**, 407 (2016).

[35] J. Bialké, T. Speck, and H. Löwen, Phys. Rev. Lett. **108**, 168301 (2012).

[36] I. Buttinoni, J. Bialké, F. Kümmel, H. Löwen, C. Bechinger, and T. Speck, Phys. Rev. Lett. **110**, 238301 (2013).

[37] G. S. Redner, M. F. Hagan, and A. Baskaran, Phys. Rev. Lett. **110**, 055701 (2013).

[38] J. Palacci, S. Sacanna, A. P. Steinberg, D. J. Pine, and P. M. Chaikin, Science **339**, 936 (2013).

[39] A. Wysocki, R. G. Winkler, and G. Gompper, EPL **105**, 48004 (2014).

[40] M. E. Cates and J. Tailleur, Annu. Rev. Condens. Matter Phys. **6**, 219 (2015).

[41] M. C. Marchetti, Y. Fily, S. Henkes, A. Patch, and D. Yllanes, Curr. Opin. Colloid Interface Sci. **21**, 34 (2016).

[42] A. Zöttl and H. Stark, J. Phys.: Condens. Matter **28**, 253001 (2016).

[43] E. M. Purcell, Am. J. Phys. **45**(1), 3 (1977).

[44] K.-T. Wu, J. B. Hishamunda, D. T. N. Chen, S. J. DeCamp, Y.-W. Chang, A. Fernández-Nieves, S. Fraden, and Z. Dogic, Science **355**, eaal1979 (2017).

[45] URL `http://blogs.brandeis.edu/science/files/2016/01/flat.jpg`.

[46] URL `http://blogs.brandeis.edu/science/files/2016/01/flat.jpg`.

[47] URL `https://microbewiki.kenyon.edu/index.php/Salmonella_enterica_NEU2011`.

[48] URL `https://justinsomnia.org/2006/06/photo-of-the-day-black-sun-in-denmarkthose-are/`.

[49] J. Elgeti, U. B. Kaupp, and G. Gompper, Biophys. J. **99**, 1018 (2010).

[50] M. J. Lighthill, Comm. Pure Appl. Math. **5**, 109 (1952).

[51] J. R. Blake, J. Fluid Mech. **46**, 199 (1971).

[52] T. Ishikawa and T. J. Pedely, J. Fluid Mech. **588**, 437 (2007).

[53] I. Llopis and I. Pagonabarraga, J. Non-Newtonian Fluid Mech. **165**, 946 (2010).

[54] M. Theers, E. Westphal, G. Gompper, and R. G. Winkler, Phys. Rev. E **93**, 032604 (2016).

[55] J. R. Howse, R. A. L. Jones, A. J. Ryan, T. Gough, R. Vafabakhsh, and R. Golestanian, Phys. Rev. Lett. **99**, 048102 (2007).

[56] F. Peruani, L. Schimansky-Geier, and M. Bär, Eur. Phys. J. Spec. Top. **191**(1), 173 (2010).

[57] P. Romanczuk, M. Bär, W. Ebeling, B. Lindner, and L. Schimansky-Geier, Eur. Phys. J. Spec. Top. **202**, 1 (2012).

[58] Y. Fily and M. C. Marchetti, Phys. Rev. Lett. **108**, 235702 (2012).

[59] B. ten Hagen, R. Wittkowski, D. Takagi, F. Kümmel, C. Bechinger, and H. Löwen, J. Phys.: Condens. Matter **27**, 194110 (2015).

[60] M. Doi and S. F. Edwards, *The Theory of Polymer Dynamics* (Clarendon Press, Oxford, 1986).

[61] M. Raible and A. Engel, Appl. Organometal. Chem. **18**, 536 (2004).

[62] R. G. Winkler, A. Wysocki, and G. Gompper, Soft Matter **11**, 6680 (2015).

[63] R. G. Winkler, Soft Matter **12**, 3737 (2016).

[64] T. Eisenstecken, G. Gompper, and R. G. Winkler, Polymers **8**, 304 (2016).

[65] A. P. Solon, M. E. Cates, and J. Tailleur, Eur. Phys. J. Spec. Top. **224**, 1231 (2015).

[66] É. Fodor, C. Nardini, M. E. Cates, J. Tailleur, P. Visco, and F. van Wijland, Phys. Rev. Lett. **117**, 038103 (2016).

[67] S. Das, G. Gompper, and R. G. Winkler, New J. Phys. **in press** (2017).

[68] H. Risken, *The Fokker-Planck Equation* (Springer, Berlin, 1989).

[69] R. Di Leonardo, L. Angelani, D. Dell'Arciprete, G. Ruocco, V. Iebba, S. Schippa, M. P. Conte, F. Mecarini, F. De Angelis, and E. Di Fabrizio, Proc. Natl. Acad. Sci. USA **107**, 9541 (2010).

[70] N. Koumakis, A. Lepore, C. Maggi, and R. Di Leonardo, Nat. Commun. **4**, 2588 (2013).

[71] J. Elgeti and G. Gompper, EPL **101**, 48003 (2013).

[72] Y. Fily, A. Baskaran, and M. F. Hagan, Soft Matter **10**, 5609 (2014).

[73] N. Koumakis, C. Maggi, and R. Di Leonardo, Soft Matter **10**, 5695 (2014).

[74] O. Sipos, K. Nagy, R. Di Leonardo, and P. Galajda, Phys. Rev. Lett. **114**, 258104 (2015).

[75] S. C. Takatori, W. Yan, and J. F. Brady, Phys. Rev. Lett. **113**, 028103 (2014).

[76] A. P. Solon, Y. Fily, A. Baskaran, M. E. Cates, Y. Kafri, M. Kardar, and J. Tailleur, Nat. Phys. **11**, 673 (2015).

[77] H. Chaté, F. Ginelli, G. Grégoire, and F. Raynaud, Phys. Rev. E **77**, 046113 (2008).

[78] M. Abkenar, K. Marx, T. Auth, and G. Gompper, Phys. Rev. E **88**, 062314 (2013).

[79] T. Vicsek, A. Czirók, E. Ben-Jacob, I. Cohen, and O. Shochet, Phys. Rev. Lett. **75**, 1226 (1995).

[80] F. Ginelli, Eur. Phys. J. Spec. Top. **225**(11), 2099 (2016).

[81] M. Theers and R. G. Winkler, Soft Matter **10**, 5894 (2014).

[82] S. Kim and S. J. Karrila, *Microhydrodynamics: principles and selected applications* (Butterworth-Heinemann, Boston, 1991), ISBN 0486317676.

[83] J. K. G. Dhont, *An Introduction to Dynamics of Colloids* (Elsevier, Amsterdam, 1996).

[84] K. Drescher, J. Dunkel, L. H. Cisneros, S. Ganguly, and R. E. Goldstein, Proc. Natl. Acad. Sci. USA **10940**, 108 (2011).

[85] T. Ishikawa, J. R. Soc. Interface **6**, 815 (2009).

[86] K. Drescher, R. E. Goldstein, and I. Tuval, Proc. Natl. Acad. Sci. USA **107**, 11171 (2010).

[87] A. Erbe, M. Zientara, L. Baraban, C. Kreidler, and P. Leiderer, J. Phys.: Condens. Matter **20**, 404215 (2008).

[88] G. Volpe, I. Buttinoni, D. Vogt, H. J. Kümmerer, and C. Bechinger, Soft Matter **7**, 8810 (2011).

[89] I. O. Götze and G. Gompper, Phys. Rev. E **82**, 041921 (2010).

[90] T. Ishikawa, M. P. Simmonds, and T. J. Pedley, Journal of Fluid Mechanics **568**, 119 (2006).

[91] A. A. Evans, T. Ishikawa, T. Yamaguchi, and E. Lauga, Phys. Fluids **23**, 111702 (2011).

[92] F. Alarcón and I. Pagonabarraga, J. Mol. Liq. **185**, 56 (2013).

[93] J. J. Molina, Y. Nakayama, and R. Yamamoto, Soft Matter **9**, 4923 (2013).

[94] T. Ishikawa and T. J. Pedley, Phys. Rev. Lett. **100**, 088103 (2008).

[95] K. Ishimoto and E. A. Gaffney, Phys. Rev. E **88**, 062702 (2013).

[96] A. Zöttl and H. Stark, Phys. Rev. Lett. **112**, 118101 (2014).

[97] M. Theers, E. Westphal, G. Gompper, and R. G. Winkler, Soft Matter **12**, 7372 (2016).

[98] S. E. Spagnolie and E. Lauga, J. Fluid Mech. **700**, 105 (2012).

[99] S. R. Keller and T. Y. Wu, J. Fluid Mech. **80**, 259 (1977).

[100] R. Matas-Navarro, R. Golestanian, T. B. Liverpool, and S. M. Fielding, Phys. Rev. E **90**, 032304 (2014).

[101] J. Blaschke, M. Maurer, K. Menon, A. Zöttl, and H. Stark, Soft Matter **12**, 9821 (2016).

[102] F. Alarcón, C. Valeriani, and I. Pagonabarraga, Soft Matter **13**, 814 (2017).

[103] N. Yoshinaga and T. B. Liverpool, Phys. Rev. E **96**, 020603 (2017).

[104] M. Theers, K. Qi, R. G. Winkler, and G. Gompper, *Hydrodynamically and sterically induced clusters of shperiodal squirmers* (2018), in preparation.

[105] F. Ginelli, F. Peruani, M. Bär, and H. Chaté, Phys. Rev. Lett **104**, 184502 (2010).

[106] C. W. Gardener, *Handbook of Stochastic Methods* (Springer, Berlin, 1983).